Segmented plasma flow meter response from kinetic simulations

Guangdong Liu, Richard Marchand

[1]University of Alberta, Department of physics, 4-181 CCIS, Edmonton, AB, T6G 2E1
[2]University of Alberta, Department of physics, 4-181 CCIS, Edmonton, AB, T6G 2E1

Key Points:

- PIC simulation
- plasma flow meter
- segmented flow meter
- space plasma

Corresponding author: Guangdong Liu, guangdon@ualberta.ca

Abstract

A relatively simple design of a segmented flow meter (SF meter) is presented for measuring in situ plasma flow velocities and other space plasma parameters. The response of the flow meter to space environment is simulated for plasma conditions representative of the ionosphere at mid and low latitudes using a Particle In Cell (PIC) code. A synthetic data set consisting of ion currents collected by several segments of the flow meter, and the physical parameters for which they were calculated, is then used to construct a solution library from which inference models can be constructed, using radial basis function (RBF) and neural network regressions. Simulation results show that with such a flow meter, it should be possible to infer plasma flow velocities in the direction perpendicular to the ram direction, with uncertainties of 45 m/s or less. Models can also be constructed to infer plasma densities, with a relative error of 23 %. This work is presented as a first assessment and proof of concept for an original design of a simple and robust flow meter.

1 Introduction

Plasma winds are a key manifestation of the dynamical processes at play in the ionosphere, including ionospheric coupling with the magnetosphere and with solid Earth. This has motivated the use of various instruments mounted on satellites to measure plasma flow velocities under different space plasma environments. In addition to affecting ground infrastructures (Pirjola, 2000), events such as magnetic storms or substorms can be responsible for satellite malfunction and, in extreme cases, total loss (Baker, 2000). These storms cause turbulence in the magnetosphere, which often result in strong currents and winds. Thus monitoring ionospheric winds provides key information for a better understanding of our near-space environment, which in turn can lead to improved mitigation measures in case of extreme events. Ionospheric winds can also provide information on solid Earth activity such as earthquakes, volcanic eruptions, or high yield underground explosions (Rudenko & Uralov, 1995; Davies & Archambeau, 1998; Krasnov & Drobzheva, 2005; Parrot et al., 2006; Parrot, 2012; Yang et al., 2012; Ryu et al., 2014; Shen et al., 2018; De Santis et al., 2019). Two types of waves are being considered in relation to earthquakes. Post seismic acoustic and gravitational waves have been observed with satellites in low Earth orbit (LEO), and their connection with solid Earth phenomena is well understood from theory and computer simulations (Rudenko & Uralov, 1995; Davies & Archambeau, 1998; Krasnov & Drobzheva, 2005; Yang et al., 2012). Direct observations and statistical analyses have also been reported to support the occurrence of electromagnetic wave signatures prior to large earthquakes (Parrot et al., 2006; Parrot, 2012; Ryu et al., 2014; Shen et al., 2018; De Santis et al., 2019). While not yet demonstrated, the possibility of observing ionospheric perturbations prior to large earthquakes remains a topic of vital interest, especially in countries located in seismically active parts of the planet (ibid).

Several designs of plasma flow meters have been used on satellites to measure ionospheric winds, including retarding potential analyzers (Hanson et al., 1973; R. A. Heelis & Hanson, 2013; Satir et al., 2015), ion drift meters (Hundhausen et al., 1967; Galperin et al., 1973; Hanson et al., 1973; Galperin et al., 1974; Hanson & Heelis, 1975; R. Heelis et al., 1981; Ogilvie et al., 1995; Reigber et al., 2003; Berthelier, Godefroy, Leblanc, Seran, et al., 2006; Stoneback et al., 2012; R. A. Heelis et al., 2017), "top hat" analyzers (C. Carlson et al., 1982; C. W. Carlson & McFadden, 2013; C. W. Carlson et al., 2001), ion imagers (Whalen et al., 1994; Yau et al., 1998; Knudsen et al., 2003; Yau et al., 2015; Knudsen et al., 2017), and segmented Langmuir probes (Séran et al., 2005; Lebreton et al., 2006; Santandrea et al., 2013). The first satellites equipped with ion drift meters were deployed in the 1960s and 1970s (Hundhausen et al., 1967; Galperin et al., 1973; Hanson et al., 1973; Galperin et al., 1974; Hanson & Heelis, 1975; R. Heelis et al., 1981). While the names differed, the working principles were similar. A simplified schematic of such

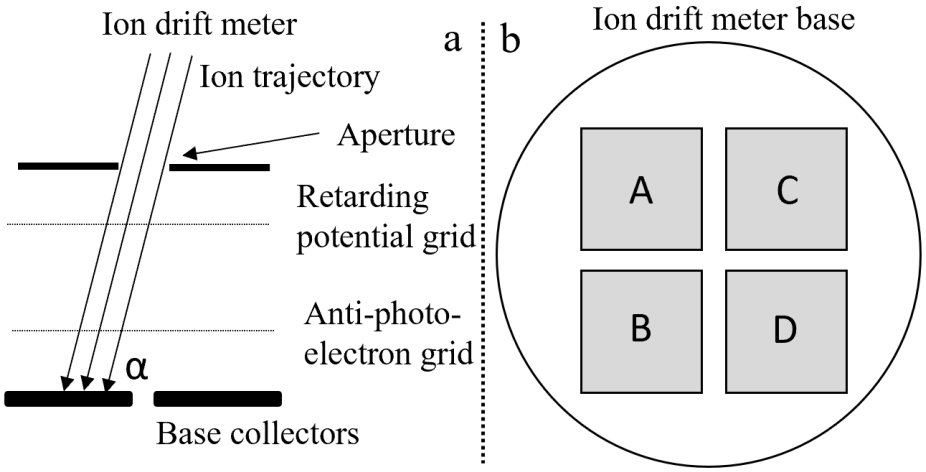

Figure 1. Illustration of an ion drift meter with integrated retarding potential analyzer. The side view in panel (a) illuminates a cross section of the aperture, grids, and collector plates. Panel (b) illustrates the four collectors at the base of the sensor.

a device is shown in Fig. 1. In this configuration, ions enter the sensor from the top aperture, and are collected by four current collectors at the base. The ram speed is measured with a retarding potential analyzer from which incoming ion masses and speeds can be determined. As shown on panel (a) of the figure, the voltage applied to the top grid is swept so as to block ions with varying energies from entering the sensor. As voltage is increased, abrupt drops are measured in the collected currents (R. A. Heelis & Hanson, 2013). The voltages at which these reductions occur, correspond to different energy to charge ratios of incoming ions, in the satellite reference frame. The magnitude and shape of these drops also provide information on ion temperatures and relative densities. The second grid is biased to a fixed negative voltage to prevent the escape of photoelectrons from the base collectors. When collectors are exposed to UV radiation, simulations suggest that most photoelectrons are reflected back to the collector from which they were emitted (Stoneback et al., 2012). The angle of incidence α of the plasma flow is determined from the relative currents collected by the segments. This, combined with the ram speed measured with the retarding potential analyzer, is used to determine the transverse flow velocity. The retarding potential analyzer/ion drift meter is robust, and it was used in many space missions. For example, VEIS on the WIND spacecraft was used to study the foreshock subsonic particles reflected from the bow shock (Ogilvie et al., 1995). This instrument can also be used to measure electron energies by reversing the analyzer electric field polarization. Similarly, IAP on DEMETER was used to measure plasma flow velocities with particular attention to the perturbed flow induced by waves caused by seismic activity (Berthelier, Godefroy, Leblanc, Seran, et al., 2006). The accuracy of ram speed measurements, obtained with IAP on DEMETER, was estimated to be approximately 10%, based on laboratory calibrations and computer simulations (Séran, 2003; Berthelier, Godefroy, Leblanc, Seran, et al., 2006). Similar flow meters are also used on spacecraft, such as Dynamics Explorer B (R. Heelis et al., 1981), C/NOFS satellite (Stoneback et al., 2012), and Ionospheric Connections Explorer (R. A. Heelis et al., 2017). A similar instrument has been developed based on the same basic principle, referred to as the "backplane design". In this configuration, ions travel to the base of the sensor and are deflected by a strong electric field, to be collected on the backside of collector segments, as illustrated in Fig. 2. This configuration was used in DIDM on the CHAMP satellite to prevent direct UV radiation from entering the collectors, and minimize perturbations from photoelectrons (Reigber et al., 2003).

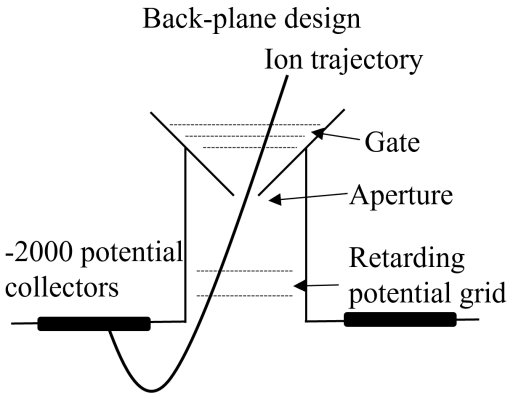

Figure 2. DIDM on the CHAMP satellite uses a back-plane design of ion drift meter. Ions are deflected 180° once they are in the detector dome using a -2000 volts potential.

The "top-hat" analyzer shown in panel a of Fig. 3 is widely used to sample charged particles over 360° in azimuthal (C. Carlson et al., 1982; C. W. Carlson & McFadden, 2013; C. W. Carlson et al., 2001). Trajectories of incoming particles are bent by a radial electric field between two hemispherical electrodes of different radii. For a given potential difference between the two hemispheres, only particles in a narrow range of energy to charge ratio can follow a trajectory leading to the base collectors. The energy spectrum of the particles is then obtained by sweeping the potential difference between the two analyzer hemispheres. The "top hat" analyzer provides a pitch-angle range over the full 2-dimensional plane through the analyzer aperture. Ion imagers are yet another type of flow meter in which, as illustrated in panel b of Fig. 3. In this configuration, ions enter through an aperture, and are dispersed by an electric field between two concentric hemispherical shields, onto a detector array, as determined by their energy to charge ratio. Depending on the setup, incoming particle velocities are measured over 180°, or the full 360° degrees in azimuthal angles. For example, the F3C Cold Plasma Analyzer (CPA) instrument on Freja can sample ions over a range of 360° in azimuthal angles around the satellite (Whalen et al., 1994). On Swarm, the Electric Field Instrument (EFI) consists of two imagers, each with 180° wide apertures, oriented perpendicularly to one another, thus providing a three-dimensional sample of incoming ion distributions (Knudsen et al., 2017). Other spacecraft are also equipped with ion imagers, including ePOP (Yau et al., 2015), and Plante-B (Yau et al., 1998). In principle, ion imagers can accurately measure ion drift velocities and ion masses without the need for sweeping voltage. The accuracy with which plasma flow velocity can be inferred with ion imagers has been assessed to be of order 20 m/s based on rocket-based measurements (Sangalli et al., 2009). In space, performance can vary due to several factors, including satellite potentials, changing plasma conditions, and aging of sensor components (Marchand et al., 2010; Knudsen et al., 2017).

Segmented Spherical Langmuir Probes have also been used to measure bulk plasma flow. The surface of the probe is divided into several equipotential spherical caps or segments facing different directions, from which individual currents are measured. The relative currents from these segments and the supporting sphere can in principle be used to infer plasma density, temperature, and plasma flow velocity (Lebreton et al., 2006). This instrument was used on satellites such as DEMETER and Proba-2 (Séran et al., 2005; Lebreton et al., 2006; Santandrea et al., 2013). It is also possible to infer plasma flow velocities indirectly from measured electric fields and the relation for the $\vec{E} \times \vec{B}$ drift. Boom-supported electric field probes are used on numerous satellite and rocket experiments, including ICE on DEMETER (Berthelier, Godefroy, Leblanc, Malingre, et

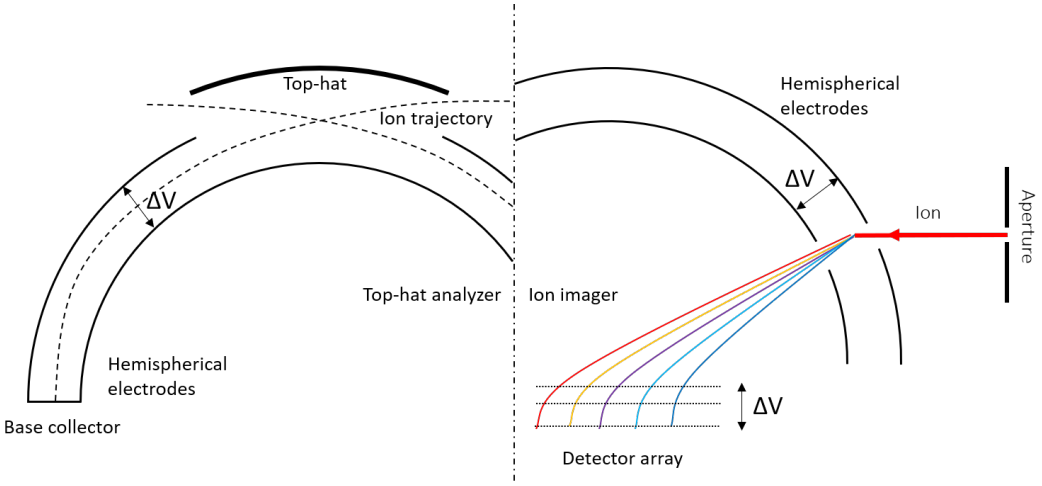

Figure 3. Illustration of a 'top hat' analyzer and ion imager. Both devices can sample ions over 360° azimuthal angles.

al., 2006) and the Fields Instrument on FAST (Ergun et al., 2001). At lower latitudes, it is also possible to measure the neural wind speed in the ram direction, from the Doppler shift in atmospheric emission lines using an interferometer with laser beams (Englert et al., 2007).

One important difference between flow meters and more familiar Langmuir probes is that several theories have been developed to interpret measurements made with the latter, while no theory exists for the former. As a result, the inference of plasma flow velocities from flow meters must rely on laboratory calibration and computer simulations. Thus the goals of this study are to i) characterize the response of a proposed simple flow meter applicable to ionospheric wind, using computer simulations, ii) construct inference models based on multivariate regression, and iii), assess their predictive skills for conditions representative of the lower ionosphere. In the remainder of this paper, we present the geometry of a plasma flow meter, which should combine simplicity, robustness, and accuracy. The performance of the proposed instrument is assessed based on a combination of synthetic data constructed with computer simulations, and multivariate regressions. The simulation techniques, the sensor geometry, and the regression approaches are presented in Section 2. Simulation results and assessments of inference skills are presented in Section 3. The final section summarizes our findings and contains some concluding remarks.

2 Methodology

The flow meter geometry considered is shown in Fig. 4. It is sufficiently compact to be mounted on small satellites such as CubeSats. In the satellite reference frame, ions are incident from the ram direction, with speeds approximately equal to the satellite orbital speed. Thus, the meter needs to be mounted on the ram face of the satellite to allow ions to enter the aperture. In the proposed design, there are a total of 19 collecting segments, from which individual currents are measured. The top ring aperture is biased to -4 V with respect to the spacecraft in order to repel electrons and attract ions into the cone. This negative voltage at the top also serves to increase the radial dispersion of entering ions. All other segments at the base are biased to $+3$ V in order to i) enhance dispersion of the ion beam penetrating the sensor, and ii) retain photoelectrons that might be emitted, should solar UV enter the cavity. Enhancing radial spread of the incident ion beam at the base should make the distribution of collected currents more

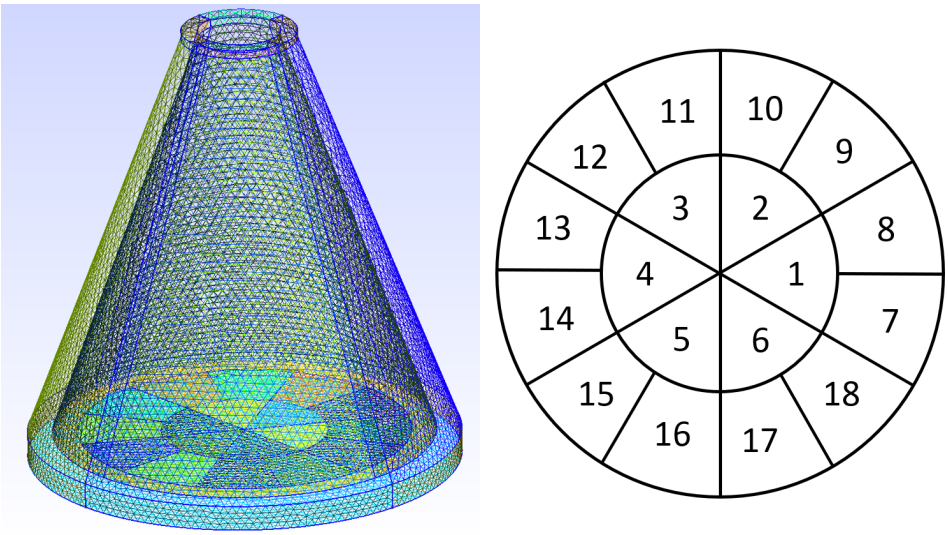

Figure 4. Illustration of the 3D geometry of the SF meter (left), and the 18 sectors at the base (right). The conical shell has a height of 5 cm, the outer radius at the base is 2.3 cm, and that at the top ring is 0.7 cm.

sensitive to the ion mass distributions and hence, to the ion effective mass. The curved conical faces of the sensor, both inside and outside, are assumed to be grounded to the satellite bus, implying that they would also be at the satellite potential V_s with respect to background plasma. Simulations indicate that if the satellite potential V_s is positive and larger than ~ 1 V, the base sensors start collecting a noticeable amount of electrons passing through the top aperture, which in turn would interfere with the measurement. In the lower ionosphere at mid and low latitudes where photoelectron and secondary electron emission are not significant, a spacecraft should be charged negatively. In the following, the proposed sensor response is assessed assuming spacecraft potentials ranging from -2 to 1 V. The following paragraphs describe the approaches used to characterize the response of the flow meter to diverse space environment conditions, to construct models to infer physical parameters of interest from measurements, and to assess their predictive skills.

2.1 Symmetry

One key feature of the device considered is symmetry. In order to characterize the response of the multiple sensors to flows with components transverse to the cone axis, we need to carry out many three-dimensional kinetic simulations assuming different plasma parameters, consisting of densities, temperatures, ion compositions, flow velocities, and satellite potentials. These simulations are used to construct a solution library consisting of collected currents by each of the 19 segments, with corresponding space-plasma conditions. Without symmetry, simulations would be required for transverse flows covering the full 360° around the sensor axis. With the six-fold rotational symmetry, and the mirror symmetry in the 18 collecting segments at the base of the sensor seen in Fig. 4, however, simulations are only needed in a much smaller 30° angular sector. For example, simulations can be carried out to calculate currents collected by all segments, for flow velocities with transverse velocities in only the 30° sector 8. These currents can then be mirror imaged with respect to the horizontal axis between sectors 7 and 8 (or 13 and 14), to extend results to transverse velocities directed in sector 7. From there, the six-fold rotational symmetry can be used to further extend our simulation results to trans-

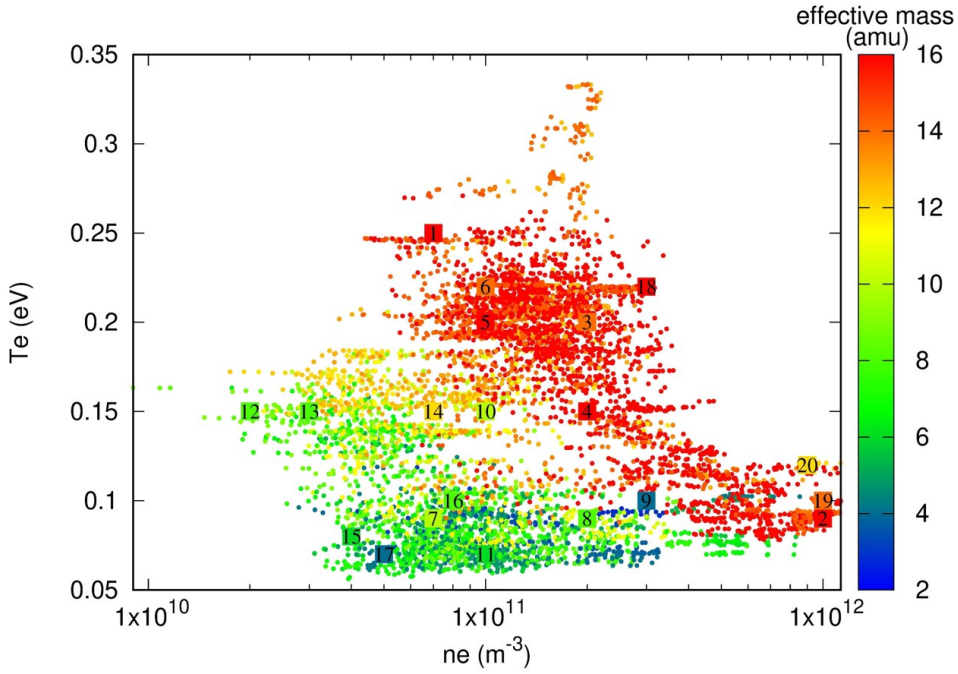

Figure 5. Scatter plot of plasma parameters obtained from the IRI model, corresponding to different latitudes, longitudes, altitudes, and times, as listed in Table 1. Numbered squares identify parameters used in the kinetic simulations.

verse velocities in all sectors, covering the full 360° of azimuthal angles; thus reducing the number of simulations by a factor 12 compared to what would be needed in the absence of symmetry.

2.2 Kinetic Simulations

The response of the sensor to different ionospheric wind conditions is simulated using the three-dimensional PIC code PTetra (Marchand, 2012; Marchand & Resendiz Lira, 2017). In this model, space is discretized with unstructured adaptive tetrahedral meshes (Frey & George, 2007; Geuzaine & Remacle, 2009), and Poisson's equation is solved at each time step, using Saad's GMRES sparse matrix solver (Saad, 2003). Electrons and ions are treated kinetically, accounting for their physical masses, and particle trajectories are calculated self-consistently using computed electric fields. The parameters assumed in the simulations have been selected so as to be representative of ionospheric conditions encountered by satellites in low Earth orbit (LEO) at mid, and low latitudes. A sample of electron and ion temperatures, electron densities, and ion mass distributions was obtained from the International Reference Ionosphere (IRI) (Bilitza et al., 2014) model for different latitudes, longitudes, altitudes, and times. The result is shown in Fig. 5, with points in the density-temperature scatter plot, and colors indicating ion effective masses. The numbered squares in the figures identify the twenty sets of plasma parameters ($T_e,\ T_i,\ n_e,\ m_{ieff}$) for which simulations were made. For each of the selected set of plasma parameters, several simulations were made for different satellite potentials, incoming plasma ram speeds, and transverse velocities distributed in the 30° sector 7, for a total of 310 simulations. When extended to the full 360° circle as described above, this produces a solution library consisting of 2676 entries used to train and assess our inference models.

For simplicity, and considering that in the conditions considered, O^+ and H^+ constituted 94% or more of all ion species, only these two ion species were considered in the

Table 1. Range of ionospheric conditions considered with the IRI model, and corresponding ranges in space plasma parameters.

Environment and plasma conditions	Parameter range
Years	1998 2001 2004 2009
Date	Jan 4 Apr 4 Jul 4 Oct 4
Latitude	$-65°$ - $+65°$ with increment of $26°$
Longitude	$0°$ - $-360°$ with increment of $30°$
Hours	0-24 with increment of 8 hours
Height	450-550 km
Ion temperature	0.07-0.12 eV
Electron temperature	0.09-0.25 eV
Effective ion mass	4-16 amu
Density	$2 \times 10^{10} - 1 \times 10^{12} \mathrm{m}^{-3}$
Ram velocity	7000 -8000 m/s
Transverse speed	0-500 m/s
Angles	0-30˚
Spacecraft potential	-2-1 eV

simulations. Earth magnetic field is not accounted for in the simulations, owing to the fact that typical ion gyroradii in the ionosphere are of order 1 m for H^+, and 4 m for O^+, which are much larger than the $\sim$ 5 cm size of the sensor considered. Secondary electron emission is ignored in the calculations because of the low electron temperatures (below 0.5 eV) encountered in the regions of interest. Photoelectron emission is also not taken into account, which is justified when the satellite is on the night side of its orbit or when the meter aperture is not exposed to solar illumination.

2.3 Multivariate regression

Given a solution library, the next step is to construct models capable of inferring plasma parameters from measurements. In the following, we describe two approaches for constructing such models, which will be applied and assessed for their inference skills in Sec. 3. Several approaches are possible, including empirical parametric fits and multivariate regressions. Here we use two regression approaches based on i) Radial Basis Functions (RBF), and ii) Deep Learning Neural Networks. In either case, two steps are involved in the construction of a model. The first step consists of training a model on a subset of the solution library; the "training set", while the second step consists of applying the trained model to a distinct data set; the validation set, consisting of the remaining subset of the library. The inference skill of the model is generally better on the training than on the validation set. Model skills applied to the training set can be improved by further refining the model, but improvements in training do not necessarily correspond to improvements in validation inferences. Beyond a certain level of refinement in training, "overfitting" occurs, and inference skill degrades for the validation set. A good model is one with the right level of refinement so as to provide the best inference skill when applied to the validation set. Let us now briefly present the two regression methods used in our study.

2.3.1 Radial Basis function

Radial basis Function is one of the most basic regression techniques, and it is applied in many fields, including image mapping, and data tracking (Buhmann, 2003). Given a set of independent vectors $\vec{X}$ and corresponding dependent vectors $\vec{Y}$, a general expression for RBF regression is given by

$$\vec{Y} = \sum_{i=1}^{n} a_i G\left(\left|\vec{X} - \vec{X}_i\right|\right), \tag{1}$$

where $\vec{Y}$ is a vector of parameters to be inferred, $\vec{X}$ is a vector consisting of independent, measured quantities, and $(\vec{X}_i, \vec{Y}_i)$ are reference nodes or pivots in the space of independent-dependent variables. G is a function of a real variable, a_i are fitting coefficients, and n is the number of pivots used in the regression. In RBF, $\vec{X}$ and $\vec{Y}$ can be vectors of different dimensions. In what follows, however, dependent variables $\vec{Y}$ will always be scalars (vectors of dimension one), and $\vec{X}$ will be vectors of different dimensions, depending on the physical parameter being inferred. In Eq. 1, the argument of G is the L^2 norm, or Euclidean distance between $\vec{X}$ and $\vec{X}_i$; whence the name "radial" in RBF. The choice of G is arbitrary, provided that, for a given set of pivots, the set of n interpolating functions in Eq. 1 be independent of one another. When constructing a regression model with RBF, the function G, and the number and distribution of pivots must be chosen so as to yield the best possible predictive skill for a given problem. Two G functions have been found to give good predictive skill for the inferred physical parameters considered. They are described with the physical parameters in Sec. 3. The number and distribution of pivots have similarly been selected so as to provide optimal accuracy when inferring dependent parameters in a validation set. Two types of cost functions have been considered, the maximum absolute error (MAE):

$$\epsilon_{abs} = Max \mid Y_{sim} - Y_{mod} \mid, \tag{2}$$

and the maximum relative error (MRE):

$$\epsilon_{rel} = Max \left| \frac{Y_{sim} - Y_{mod}}{Y_{mod}} \right|, \tag{3}$$

calculated over a given data set, where Y_{sim} are known plasma parameters used in the simulation such as density, and Y_{mod} are the model-inferred parameters.

In order to carry out this task and construct a model, the fitting coefficients a_i in Eq. 1 have to be determined. This is done first by requiring collocation of inferred and known parameters at pivots; that is, by solving the set of equations

$$\sum_{j=1}^{N} a_j G(|\vec{X}_i - \vec{X}_j|) = \vec{Y}_{i,sim},\ i = 1, N. \tag{4}$$

Given a training data set of $\mathcal{N}$ nodes, the selection of N pivots is made by constructing models for all possible $\mathcal{N}$ choose N combinations of pivots among the $\mathcal{N}$ nodes, and selecting the one which minimizes the cost function. When the best distribution of pivots is found, the model can be further improved by relaxing collocation, by allowing for small deviations from the $\vec{Y}_{i,sim}$ and minimizing the cost functions with respect to these deviations. Yet another improvement is to go over all $\mathcal{N}$ choose N possible combinations of pivots in parallel on n multiple processors, in such a way that each processor goes through different combinations. In this case, each processor finds its unique best combination of pivots. One obvious advantage of this is an increase in speed. Another one is that relaxation, or accounting for the "nugget effect", can be applied to each of the distinct n best combinations, and selecting the combination which, after relaxation, produces the smallest cost function. It is found that the best combination then, is not necessarily the one that minimizes the cost function before relaxation. With this strategy, and using several processors, it is possible to reduce the cost function in a training set by several %, compared to a minimization made without relaxation.

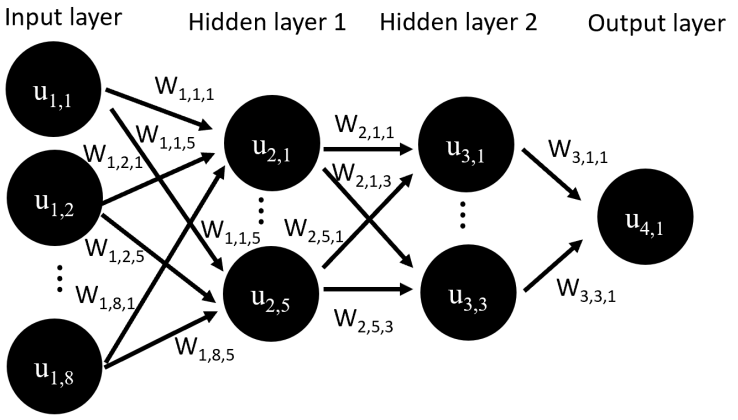

Figure 6. Schematic of a feedforward neural network.

Given the size of the data, $\mathcal{N}$ choose N can be very large. One strategy is to combine RBF with the Monte Carlo method to do a non-exhaustive search for the model. In this approach, a small subset (e.g. 100 entries) is picked each time randomly from the training data set to train a model, then the model is applied to the entire training data set to calculate the cost function. The best model is selected after a certain time and it is applied to the validation data set to determine the validation error.

2.3.2 Neural network

Neural networks have increasingly been proven useful in many applications, including plasma physics and space physics (Barkhatov & Revunov, 2010; Breuillard et al., 2020). In this work, we use the feedforward deep learning networks to infer plasma parameters from currents collected from the 19 segments in the proposed flow meter. An illustration of a feedforward network is shown in Fig. 6, with the input layer, hidden layers, and the output layer. In our problem, each node in the input layer is assigned a current from one of the segments. Node j in layer i is assigned a value $u_{i,j}$, and each node of the next layer $i+1$ is "fed" by all the nodes of the previous layer according to

$$u_{i+1,k} = \sum_{j=1}^{n_i} w_{i,j,k} f(u_{i,j} + b_{i,j}), \tag{5}$$

where $w_{i,j,k}$ are weight factors, $b_{i,j}$ are bias terms, and f is a nonlinear activation function. In this study, the bias terms are all set to zero. The w coefficients are first generated using the Monte Carlo method, and then gradient descent is used to further decrease the cost function over the training data. Training sets consisting of 500 data entries are used to train neural network models. As with RBF, many models are trained before the final model is selected. The models are then applied to the validation data sets to obtain the validation error.

2.4 Noise

Given a trained model, the skill and robustness of inference are tested against noise in the validation sets. Noise in collected currents can be statistical in nature, or it can be associates with physical processes such as waves and turbulence. The current collected by a segment is given by the number of particles N collected in a given sampling time τ, multiplied by their respective charges, and divided by τ; that is, assuming singly ion-

ized ions for simplicity,

$$I = \frac{Ne}{\tau}. \tag{6}$$

Owing to the discrete nature of this process, the number N follows approximately Poisson statistics. The standard deviation; that is, the noise level, in N is therefore approximately the square root of $\bar{N}$, the average value of N: $\sigma_N \simeq \sqrt{\bar{N}}$. Thus, it follows that the standard deviation in the collected current is approximately

$$\sigma_I \simeq \frac{\sigma_N e}{\tau} \simeq \sqrt{\frac{Ie}{\tau}}. \tag{7}$$

In simulations however, the number of simulation particles N_s accounted for, is generally smaller than the actual number of physical particles in a plasma. In order to account for that, simulation particles carry a statistical weight w, corresponding to the number of actual particles that they "represent". Currents calculated in simulations are therefore obtained by multiplying the charge of each collected particle by its statistical weight as in

$$I = \frac{wN_s e}{\tau}, \tag{8}$$

and the resulting standard deviation in the current calculated in a simulation is

$$\sigma_I \simeq \frac{w\sigma_N e}{\tau} \simeq \sqrt{\frac{wIe}{\tau}}. \tag{9}$$

The standard deviation in the collected current can also be calculated directly from our simulation results, by considering a case with zero transverse flow velocity. In this case, by symmetry, all six inner segments should collect the same current, as should the twelve outer segments. Thus, calculating the standard deviation in these currents provides an estimate of the intrinsic statistical noise in the current collected by a single segment. For example, in one of the simulations, using a sampling time of 1μs, in which ions have a statistical weight $w = 2$, the average current per inner segment is calculated to be $I \simeq 2n$A. In this case, the standard deviation of the current over the six segments is found to be $\simeq 29p$A, which is in good agreement with the $25p$A estimated from Eq. 9.

In order to test the robustness of our models, additional noise is introduced in our validation sets, in addition to the intrinsic statistical noise mentioned above. Here again, this added noise is assumed to be proportional to the square root of the collected current as per

$$I_\sigma = I_0 \left(1 + r\sigma\sqrt{\frac{I_0}{1n\text{A}}}\right), \tag{10}$$

where I_σ is the current collected with added noise, I_0 is the simulated collected current from the solution library for a given segment, σ is a relative standard deviation, and r is a zero-mean random number with Gaussian distribution and unit standard deviation. For each value of σ, 100 sets of random noise have been used to calculate the averages of the maximum errors and Root-Mean-Squared (RMS) errors reported in Tables 3.

3 Results and discussion

We now proceed with the construction of models for selected plasma parameters.

3.1 Transverse flow velocity

The inference of transverse velocities relies on the symmetry and the currents collected by the base 18 segments as described above. This is made in two steps in which i) the direction of the transverse flow velocity, and ii) its magnitude are determined.

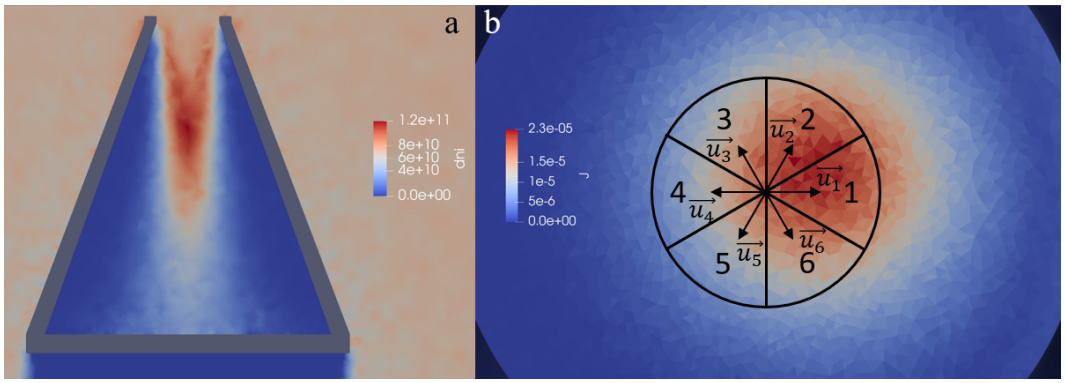

Figure 7. Cross section of the ion density in and out of the SF meter (a), and collected current density profile at the base (b). The density is in units of m^{-3}, and current density in units of Am^{-2}. This corresponds to condition 14 in Fig. 5, with n_e, m_{ieff}, T_e, T_i being 7×10^{10} m^{-3}, 12 amu, 0.15 eV and 0.11 eV respectively.

Table 2. Examples of transverse wind angles obtained from $\vec{U}$ in the vector approach. Each run number corresponding to a set of plasma conditions mentioned in section 2.2. "Simulation", "Inner", and "Outer" corresponding to the inner ring vector, outer ring vector and the wind direction used in the simulation.

Plasma condition#	Wind speed (m/s)	Simulation	Inner	Outer
1	125	10°	18.8°	17.6°
1	250	10°	12.2°	13.0°
1	375	10°	12.4°	12.2°
1	500	10°	10.5°	11.9°
2	125	20°	28.4°	30.8°
2	250	20°	23.7°	23.6°
2	375	20°	23.3°	23.0°
2	500	20°	21.0°	22.8°

3.1.1 Transverse flow direction - The vector approach

An obvious manifestation of a transverse flow velocity in incident plasma is an azimuthal asymmetry in the currents collected at the base of the sensor, as shown in Fig. 7. Given the geometry of the sensor, the shift in the centroid of the collected current must be in the direction of the transverse plasma flow velocity. This shift in turn can be determined from the average of the unit vector pointing in the middle of each sector, as shown in panel b of Fig. 7, weighted with the current that it collects. In practice, two averages are made, for the inner sectors as

$$\vec{U}_1 = \sum_{i=1}^{6} \vec{u_i} \cdot I_i, \tag{11}$$

and a similar expression is used for $\vec{U}_2$, calculated with the 12 outer sectors. The direction of the two vectors give indications of directions of the wind, as shown in Table 2. These vectors are then combined linearly as:

$$\vec{U} = (1-\alpha)\vec{U}_1 + \alpha\vec{U}_2, \tag{12}$$

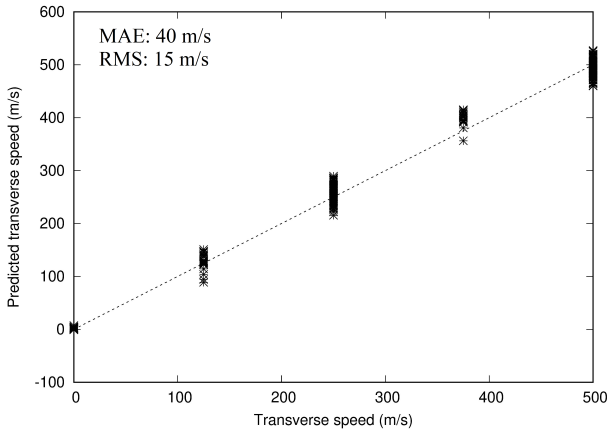

Figure 8. Correlation plot of the transverse wind speeds inferred for the validation set, vs. actual speeds used in the simulations. For reference, the dotted line corresponds to a perfect correlation. In this case, RBF is used with 5 pivots, leading to a maximum absolute error (MAE) of 40 m/s, and a RMS error of 15 m/s.

Table 3. Errors in inferred angles, transverse speeds, velocities, and densities calculated without, and with noise added to currents in the validation set.

Parameter:	Angle (°)	Speed (m/s)	Velocity (m/s)	Density (%)
Method:	Vector	RBF	Vector+RBF	RBF
Skill metric:	RMS	RMS	RMS	RMSrE
$\sigma = 0$	3.2	15	20	11
$\sigma = 1\%$	3.6	16	20	12
$\sigma = 2\%$	4.2	17	21	12
Skill metric:	MAE	MAE	MAE	MRE
$\sigma = 0$	10.7	40	45	23
$\sigma = 1\%$	15	52	58	32
$\sigma = 2\%$	20	70	75	49

where the parameter α is selected so as to minimize the absolute error in the inferred transverse velocity over a given training data set. $\alpha \simeq 0.94$ is found to be optimal in all cases considered, and it is the value used in the inference models considered below.

3.1.2 Transverse flow speed and velocity

Given a direction of the flow from Eq. 12, the transverse velocity can then be obtained from the transverse speed. The speed is inferred using RBF regression, in which the magnitudes of $\vec{U}_1$ and $\vec{U}_2$ are used as the two components of independent vectors $\vec{X}$. For example, a correlation plot of inferred speeds as a function of the actual speed from the solution library is shown in Fig. 8. In this case, the model is constructed on a training set of 1338 randomly selected nodes from the solution library, using five pivots as explained in Sec. 2.3.1, and it is applied to a validation set consisting of the 1338 remaining nodes. The regression function used here is $G(x) = 0.5x^{1.6} \times log(x^2)$ for $x > 0$ and the cost function is the maximum absolute error over the set considered. The figure also shows the value of the cost function (40 m/s) and the RMS error (15 m/s) computed on

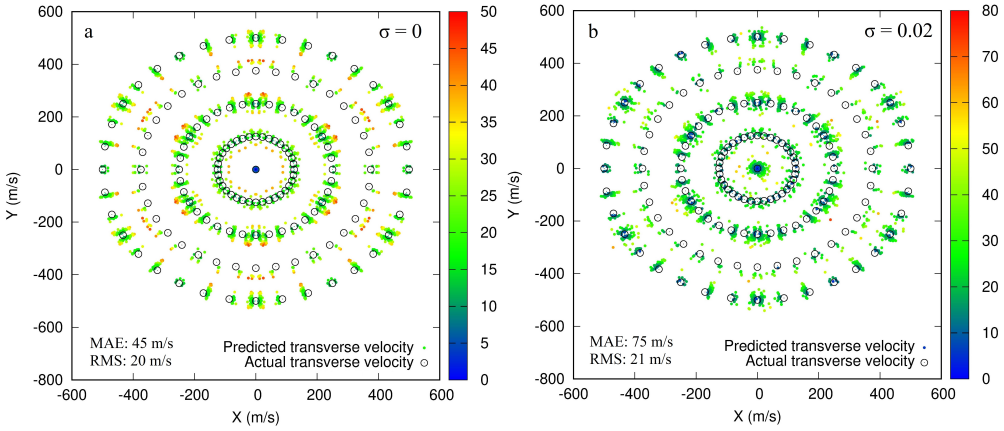

Figure 9. Actual and inferred transverse velocities without (a) and with (b) 2% added noise in the validation data set. The color scale shows the absolute errors in the model velocity predictions. Inferred velocities were obtained with RBF regression, using 5 pivots.

the validation set. Figure 9 shows RBF predicted transverse predicted and actual transverse flow velocities without (left) and with (right) 2% ($\sigma = 0.02$) added statistical noise in the validation set using Eq. 10. Here the model uses the same training and validation sets as for Fig. 8. When the model is applied to the validation set, the maximum absolute error, and root-mean-squared error are 45 m/s and 20 m/s respectively, when no noise is added. These errors increase respectively to 75 m/s, and 21 m/s when 2% relative noise is added to the validation set, which corresponds to approximately 72% of the simulation statistical noise estimated from Eq. 9. Results from neural network, not shown here, are comparable within 30%, with RBF prediction being slightly more accurate. More inference skill metrics are listed in Table 3, for different levels of added noise. As expected, our model predictive skill decreases as noise is added, and the maximum absolute error is found to increase by a factor two for a level of added noise of approximately 2%.

3.2 Density Prediction

While our primary objective is to infer ionospheric plasma flow velocities, it is interesting to explore the possibility for the proposed instrument to be used to infer other physical quantities. This is motivated by the fact that the currents collected by the many segments in the meter, and their relative values, are sensitive to several satellite plasma environment parameters, including ion densities and masses, ion temperatures, ram, and transverse velocities, and satellite potentials. Models were constructed for the plasma density using both RBF and neural network regression, and both are found to yield inferences with comparable skills. Here, however, considering the nearly two orders of magnitude range over which densities vary in our solution library and the fact that the density is a positive definite quantity, the cost function chosen in the construction of the models consists of the maximum relative error (in absolute value) over the training data set. This is preferred to the absolute error because, with the latter, models can be constructed with excellent skills for the larger densities, but poor ones for lower densities. Among the several G functions tested, the best one for predicting density was $g(\mathbf{x}) = \mathbf{x}^5$. Here, 5 pivots were used as a good balance between training and validation inference skills. 500 entries were used to train models using neural networks, with a four-layer network with 19, 15, 7, and 1 nodes. Figure 10 shows correlation plots of inferred density, as a function of actual densities obtained with neural network (left) and RBF (right) regression,

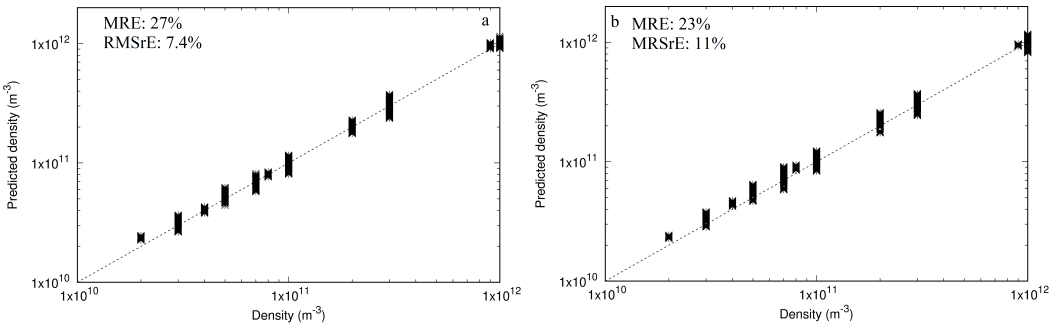

Figure 10. Predicted densities vs. densities used in simulation obtained by minimizing the maximum relative error. The neural network prediction with 500 points is shown on the left (relative error 27%) and the RBF predicted density using 5 pivots is shown on the right (relative error 23%). The dotted line corresponds to a perfect correlation between predictions and actual densities.

for the validation set without the addition of statistical noise. Both regression techniques yield comparable predictive skills, with maximum relative errors of 27% and 23%, and root-mean-square relative errors of 7.4% and 11% respectively for the neural network and RBF. As for the transverse flow velocity, the models' robustness to statistical noise was assessed by adding random noise to the currents collected by each segment, as per Eq. 10. The impact on predictive skills is given in Table 3, which again shows a degradation of skill with an increase in the level of noise.

4 Summary and conclusion

Results are presented for a particle sensor, which could be mounted on satellites, to infer in situ transverse plasma flow velocities. The device consists of several electrically biased segments at the base of a conical enclosure, and a circular ring on the top aperture, from which currents are measured. Three-dimensional kinetic particle in cell (PIC) simulations are made to construct a solution library and data sets, for plasma environment conditions of relevance to satellites in low Earth orbit. The symmetry of the device enables the construction of data sets for transverse velocities directed in the full 360° in the plane perpendicular to the ram direction of plasma flow velocities, from simulations made in only a 30° sector. Owing to the large computational resources required to carry out kinetic simulations, symmetry is key in reducing the required number of simulations. Training and validation data sets, constructed with our solution library, are used to construct regression models capable of inferring transverse velocities and plasma densities. Two approaches are assessed for constructing such models, consisting of radial basis function, and neural network regressions. The two approaches are found to have comparable skills for inferring both transverse velocities, and plasma densities. With the configuration considered, it was not possible to make an accurate inference of the plasma flow speed in the ram direction, because variations in that speed have a similar effect to variations in the plasma density. Better inference of the ram speed should nonetheless be achievable by using a separate, or integrated retarding potential analyzer as illustrated in Fig. 1.

The level of statistical noise in the collected currents, associated with the discrete nature of kinetic simulations, explains in part the relatively small discrepancies between our model predictions and actual values in the data sets. Considering that simulations are made with significantly fewer particles than there would be in an actual plasma, the

statistical uncertainties in our simulated currents are larger than those that would occur in space under similar conditions. The tolerance of our models to statistical noise is assessed by adding varying levels of normally distributed noise to the currents in our validation sets, in addition to the numerical simulation noise mentioned above. The skill of both RBF and neural network regressions decreases as noise is added, and it is estimated that an additional 2% relative noise leads only to approximately doubling in the uncertainty of model inferences in both cases.

Several approximations were made in the simulations used to construct our training and validation sets. In particular, the presence of a satellite bus was not taken into account, which is justified if the flow meter is mounted on the ram face of a satellite, and the fact that satellites in low Earth orbit have supersonic ram velocities. The geomagnetic field was also neglected, which is justified by the fact that typical ion thermal ion gyro-radii is a factor 10 or more, larger than the size of the sensor. The neglect of solar illumination and photoelectron emission is valid when the satellite is on the night side of its orbit. When the satellite is sunlit, however, it would be possible for the negatively biased ring at the sensor aperture, to emit photoelectrons which, owing to the negative bias, would be repelled, and appear as collected positive current. Solar UVs could also enter the aperture and reach directly, or indirectly through multiple reflections, the positively biased segments. This in turn would result in photoelectrons being emitted inside the flow meter which, owing to the positive bias of the segments at the base, would likely be attracted back to the segments, albeit, not necessarily at the exact position where they were emitted. This, and the exposition of the positive ring at the aperture, would likely affect measured currents, and require corrections in the models presented above to infer plasma parameters. These effects should be included in models constructed to support missions, in which specific spacecraft geometry, orbital parameters, and expected range of plasma environment parameters would be taken into account. Such an analysis is of course well beyond the scope of this preliminary study, as it would require accounting for a broader range of parameters and environmental conditions, and would require significantly more simulations. Considering the investment and years of preparation preceding a launch, such an investment, enabling better data acquisition, should nonetheless be well justified.

Acknowledgments

This work was supported by the China Scholarship Council (CSC) and the Natural Sciences and Engineering Research Council of Canada. The kinetic simulations used in this study were made on the Compute Canada computing infrastructure. Simulation data can be accessed through `https://zenodo.org/record/4434879#.X_4BAdhKhPZ` (Liu, 2021).

References

Baker, D. (2000). The occurrence of operational anomalies in spacecraft and their relationship to space weather. *IEEE Transactions on Plasma Science*, *28*(6), 2007–2016. Retrieved from `http://ieeexplore.ieee.org/document/902228/` doi: 10.1109/27.902228

Barkhatov, N. A., & Revunov, S. E. (2010, dec). Neural network classification of discontinuities in space plasma parameters. *Geomagnetism and Aeronomy*, *50*(7), 894–904. Retrieved from `http://link.springer.com/10.1134/S001679321007011X` doi: 10.1134/S001679321007011X

Berthelier, J., Godefroy, M., Leblanc, F., Malingre, M., Menvielle, M., Lagoutte, D., ... Pfaff, R. (2006, apr). ICE, the electric field experiment on DEMETER. *Planetary and Space Science*, *54*(5), 456–471. Retrieved from `https://linkinghub.elsevier.com/retrieve/pii/S0032063305002072` doi: 10.1016/j.pss.2005.10.016

Berthelier, J., Godefroy, M., Leblanc, F., Seran, E., Peschard, D., Gilbert, P., & Artru, J. (2006, apr). IAP, the thermal plasma analyzer on DEMETER. *Planetary and Space Science*, *54*(5), 487–501. Retrieved from https://linkinghub.elsevier.com/retrieve/pii/S0032063305002096 doi: 10.1016/j.pss.2005.10.018

Bilitza, D., Altadill, D., Zhang, Y., Mertens, C., Truhlik, V., Richards, P., ... Reinisch, B. (2014, feb). The International Reference Ionosphere 2012 – a model of international collaboration. *Journal of Space Weather and Space Climate*, *4*, A07. Retrieved from http://www.swsc-journal.org/10.1051/swsc/2014004 doi: 10.1051/swsc/2014004

Breuillard, H., Dupuis, R., Retino, A., Le Contel, O., Amaya, J., & Lapenta, G. (2020, sep). Automatic Classification of Plasma Regions in Near-Earth Space With Supervised Machine Learning: Application to Magnetospheric Multi Scale 2016–2019 Observations. *Frontiers in Astronomy and Space Sciences*, *7*. Retrieved from https://www.frontiersin.org/article/10.3389/fspas.2020.00055/full doi: 10.3389/fspas.2020.00055

Buhmann, M. D. (2003). *Radial basis functions: theory and implementations* (Vol. 12). Cambridge university press.

Carlson, C., Curtis, D., Paschmann, G., & Michel, W. (1982, jan). An instrument for rapidly measuring plasma distribution functions with high resolution. *Advances in Space Research*, *2*(7), 67–70. Retrieved from https://linkinghub.elsevier.com/retrieve/pii/027311778290151X doi: 10.1016/0273-1177(82)90151-X

Carlson, C. W., & McFadden, J. P. (2013, mar). Design and Application of Imaging Plasma Instruments. In *Geophysical monograph series* (Vol. 102, pp. 125–140). Retrieved from http://doi.wiley.com/10.1029/GM102p0125 doi: 10.1029/GM102p0125

Carlson, C. W., Mcfadden, J. P., Turin, P., Curtis, D. W., & Magoncelli, A. (2001). The electron and ion plasma experiment for FAST. *Space Science Reviews*, *98*(1-2), 33–66. doi: 10.1023/A:1013139910140

Davies, J. B., & Archambeau, C. B. (1998, jan). Modeling of atmospheric and ionospheric disturbances from shallow seismic sources. *Physics of the Earth and Planetary Interiors*, *105*(3-4), 183–199. Retrieved from https://linkinghub.elsevier.com/retrieve/pii/S0031920197000903 doi: 10.1016/S0031-9201(97)00090-3

De Santis, A., Marchetti, D., Pavón-Carrasco, F. J., Cianchini, G., Perrone, L., Abbattista, C., ... Haagmans, R. (2019, dec). Precursory worldwide signatures of earthquake occurrences on Swarm satellite data. *Scientific Reports*, *9*(1), 20287. Retrieved from http://www.nature.com/articles/s41598-019-56599-1 doi: 10.1038/s41598-019-56599-1

Englert, C. R., Babcock, D. D., & Harlander, J. M. (2007, oct). Doppler asymmetric spatial heterodyne spectroscopy (DASH): concept and experimental demonstration. *Applied Optics*, *46*(29), 7297. Retrieved from https://www.osapublishing.org/abstract.cfm?URI=ao-46-29-7297 doi: 10.1364/AO.46.007297

Ergun, R. E., Carlson, C. W., Mozer, F. S., Delory, G. T., Temerin, M., Mcfadden, J. P., ... Cattell, C. A. (2001). The fast satellite fields instrument. *Space Science Reviews*, *98*(1-2), 67–91. doi: 10.1023/A:1013131708323

Frey, P., & George, P. L. (2007). *Mesh Generation: Application to Finite Elements*. London, UK: ISTE.

Galperin, Y., Ponomarev, V., & Zosimova, A. (1973, oct). *Direct measurements of ion drift velocity in the upper ionosphere during a magnetic storm. Part 1: Experiment description and some results of measurements during magnetically quiet time.*

Galperin, Y., Ponomarev, V. N., & Zosimova, A. G. (1974). Plasma convection in

polar ionosphere. *Annales de Geophysique*, *30*(1), 1–7.

Geuzaine, C., & Remacle, J.-F. (2009, sep). Gmsh: A 3-D finite element mesh generator with built-in pre- and post-processing facilities. *International Journal for Numerical Methods in Engineering*, *79*(11), 1309–1331. Retrieved from http://doi.wiley.com/10.1002/nme.2579 doi: 10.1002/nme.2579

Hanson, W. B., & Heelis, R. A. (1975, nov). Techniques for measuring bulk gas-motions from satellites. *Space Science Instrumentation*, *1*, 493–524.

Hanson, W. B., Zuccaro, D. R., Lippincott, C. R., & Sanatani, S. (1973, apr). The retarding-potential analyzer on Atmosphere Explorer. *Radio Science*, *8*(4), 333–339. Retrieved from http://doi.wiley.com/10.1029/RS008i004p00333 doi: 10.1029/RS008i004p00333

Heelis, R., Hanson, W., Lippincott, C., Zuccaro, D., Harmon, L., Holt, B., ... Power, R. (1981, dec). The Ion Drift Meter for Dynamics Explorer-B. *Space Science Instrumentation*, *5*, 511–521.

Heelis, R. A., & Hanson, W. B. (2013, mar). Measurements of Thermal Ion Drift Velocity and Temperature Using Planar Sensors. In *Geophysical monograph series* (Vol. 102, pp. 61–71). American Geophysical Union (AGU). Retrieved from https://agupubs.onlinelibrary.wiley.com/doi/abs/10.1029/GM102p0061http://doi.wiley.com/10.1029/GM102p0061 doi: 10.1029/GM102p0061

Heelis, R. A., Stoneback, R. A., Perdue, M. D., Depew, M. D., Morgan, W. A., Mankey, M. W., ... Holt, B. J. (2017, oct). Ion Velocity Measurements for the Ionospheric Connections Explorer. *Space Science Reviews*, *212*(1-2), 615–629. doi: 10.1007/s11214-017-0383-3

Hundhausen, A. J., Asbridge, J. R., Bame, S. J., Gilbert, H. E., & Strong, I. B. (1967). Vela 3 satellite observations of solar wind ions: A preliminary report. *Journal of Geophysical Research*, *72*(1), 87. Retrieved from http://doi.wiley.com/10.1029/JZ072i001p00087 doi: 10.1029/JZ072i001p00087

Knudsen, D. J., Burchill, J. K., Berg, K., Cameron, T., Enno, G. A., Marcellus, C. G., ... King, R. A. (2003, jan). A low-energy charged particle distribution imager with a compact sensor for space applications. *Review of Scientific Instruments*, *74*(1), 202–211. Retrieved from http://aip.scitation.org/doi/10.1063/1.1525869 doi: 10.1063/1.1525869

Knudsen, D. J., Burchill, J. K., Buchert, S. C., Eriksson, A. I., Gill, R., Wahlund, J., ... Moffat, B. (2017, feb). Thermal ion imagers and Langmuir probes in the Swarm electric field instruments. *Journal of Geophysical Research: Space Physics*, *122*(2), 2655–2673. Retrieved from https://onlinelibrary.wiley.com/doi/abs/10.1002/2016JA022571 doi: 10.1002/2016JA022571

Krasnov, V., & Drobzheva, Y. (2005, jul). The acoustic field in the ionosphere caused by an underground nuclear explosion. *Journal of Atmospheric and Solar-Terrestrial Physics*, *67*(10), 913–920. Retrieved from https://linkinghub.elsevier.com/retrieve/pii/S1364682605000647 doi: 10.1016/j.jastp.2005.02.014

Lebreton, J.-P., Stverak, S., Travnicek, P., Maksimovic, M., Klinge, D., Merikallio, S., ... Salaquarda, M. (2006, apr). The ISL Langmuir probe experiment processing onboard DEMETER: Scientific objectives, description and first results. *Planetary and Space Science*, *54*(5), 472–486. Retrieved from https://linkinghub.elsevier.com/retrieve/pii/S0032063305002084 doi: 10.1016/j.pss.2005.10.017

Liu, G. (2021, jan). *Segmented flow meter data.* Zenodo. Retrieved from https://doi.org/10.5281/zenodo.4434879 doi: 10.5281/zenodo.4434879

Marchand, R. (2012, feb). PTetra, a Tool to Simulate Low Orbit Satellite–Plasma Interaction. *IEEE Transactions on Plasma Science*, *40*(2), 217–229. Retrieved from http://ieeexplore.ieee.org/document/6069605/ doi: 10.1109/TPS.2011.2172638

Marchand, R., Burchill, J. K., & Knudsen, D. J. (2010, oct). Modelling Electrostatic Sheath Effects on Swarm Electric Field Instrument Measurements. *Space Science Reviews*, *156*(1-4), 73–87. Retrieved from http://link.springer.com/10.1007/s11214-010-9735-y doi: 10.1007/s11214-010-9735-y

Marchand, R., & Resendiz Lira, P. A. (2017, apr). Kinetic Simulation of Spacecraft–Environment Interaction. *IEEE Transactions on Plasma Science*, *45*(4), 535–554. Retrieved from http://ieeexplore.ieee.org/document/7888602/ doi: 10.1109/TPS.2017.2682229

Ogilvie, K. W., Chornay, D. J., Fritzenreiter, R. J., Hunsaker, F., Keller, J., Lobell, J., ... Gergin, E. (1995, feb). SWE, a comprehensive plasma instrument for the WIND spacecraft. *Space Science Reviews*, *71*(1-4), 55–77. Retrieved from http://link.springer.com/10.1007/BF00751326 doi: 10.1007/BF00751326

Parrot, M. (2012, apr). Statistical analysis of automatically detected ion density variations recorded by DEMETER and their relation to seismic activity. *Annals of Geophysics*, *55*(1), 149–155. Retrieved from https://www.annalsofgeophysics.eu/index.php/annals/article/view/5270 doi: 10.4401/ag-5270

Parrot, M., Berthelier, J., Lebreton, J., Sauvaud, J., Santolik, O., & Blecki, J. (2006, jan). Examples of unusual ionospheric observations made by the DEMETER satellite over seismic regions. *Physics and Chemistry of the Earth, Parts A/B/C*, *31*(4-9), 486–495. Retrieved from https://linkinghub.elsevier.com/retrieve/pii/S147470650600043X doi: 10.1016/j.pce.2006.02.011

Pirjola, R. (2000). Geomagnetically induced currents during magnetic storms. *IEEE Transactions on Plasma Science*, *28*(6), 1867–1873. doi: 10.1109/27.902215

Reigber, C., Lühr, H., & Schwintzer, P. (Eds.). (2003). *First CHAMP Mission Results for Gravity, Magnetic and Atmospheric Studies*. Berlin, Heidelberg: Springer Berlin Heidelberg. Retrieved from http://link.springer.com/10.1007/978-3-540-38366-6 doi: 10.1007/978-3-540-38366-6

Rudenko, G., & Uralov, A. (1995, mar). Calculation of ionospheric effects due to acoustic radiation from an underground nuclear explosion. *Journal of Atmospheric and Terrestrial Physics*, *57*(3), 225–236. Retrieved from https://linkinghub.elsevier.com/retrieve/pii/0021916993E0003R doi: 10.1016/0021-9169(93)E0003-R

Ryu, K., Lee, E., Chae, J. S., Parrot, M., & Pulinets, S. (2014, oct). Seismo-ionospheric coupling appearing as equatorial electron density enhancements observed via DEMETER electron density measurements. *Journal of Geophysical Research: Space Physics*, *119*(10), 8524–8542. Retrieved from http://doi.wiley.com/10.1002/2014JA020284 doi: 10.1002/2014JA020284

Saad, Y. (2003). *Iterative Methods for Sparse Linear Systems* (Second ed.). Society for Industrial and Applied Mathematics. Retrieved from https://epubs.siam.org/doi/abs/10.1137/1.9780898718003http://epubs.siam.org/doi/book/10.1137/1.9780898718003 doi: 10.1137/1.9780898718003

Sangalli, L., Knudsen, D. J., Larsen, M. F., Zhan, T., Pfaff, R. F., & Rowland, D. (2009, apr). Rocket-based measurements of ion velocity, neutral wind, and electric field in the collisional transition region of the auroral ionosphere. *Journal of Geophysical Research: Space Physics*, *114*(A4), n/a–n/a. Retrieved from http://doi.wiley.com/10.1029/2008JA013757 doi: 10.1029/2008JA013757

Santandrea, S., Gantois, K., Strauch, K., Teston, F., Tilmans, E., Baijot, C., ... Zender, J. (2013, aug). PROBA2: Mission and Spacecraft Overview. *Solar Physics*, *286*(1), 5–19. Retrieved from http://link.springer.com/10.1007/s11207-013-0289-5 doi: 10.1007/s11207-013-0289-5

Satir, M., Sik, F., Turkoz, E., & Celik, M. (2015, jun). Design of the retard-

ing potential analyzer to be used with BURFIT-80 Ion thruster and validation using PIC-DSMC code. In *2015 7th international conference on recent advances in space technologies (rast)* (pp. 577–582). IEEE. Retrieved from http://ieeexplore.ieee.org/document/7208410/ doi: 10.1109/RAST.2015.7208410

Séran, E. (2003). Reconstruction of the ion plasma parameters from the current measurements: Mathematical tool. *Annales Geophysicae*, *21*(5), 1159–1166. Retrieved from http://www.ann-geophys.net/21/1159/2003/ doi: 10.5194/angeo-21-1159-2003

Séran, E., Berthelier, J.-J., Saouri, F. Z., & Lebreton, J.-P. (2005, jul). The spherical segmented Langmuir probe in a flowing thermal plasma: numerical model of the current collection. *Annales Geophysicae*, *23*(5), 1723–1733. Retrieved from https://angeo.copernicus.org/articles/23/1723/2005/ doi: 10.5194/angeo-23-1723-2005

Shen, X. H., Zhang, X. M., Yuan, S. G., Wang, L. W., Cao, J. B., Huang, J. P., ... Dai, J. P. (2018, may). The state-of-the-art of the China Seismo-Electromagnetic Satellite mission. *Science China Technological Sciences*, *61*(5), 634–642. Retrieved from http://link.springer.com/10.1007/s11431-018-9242-0 doi: 10.1007/s11431-018-9242-0

Stoneback, R. A., Davidson, R. L., & Heelis, R. A. (2012, aug). Ion drift meter calibration and photoemission correction for the C/NOFS satellite. *Journal of Geophysical Research: Space Physics*, *117*(A8), n/a–n/a. Retrieved from http://doi.wiley.com/10.1029/2012JA017636 doi: 10.1029/2012JA017636

Whalen, B. A., Knudsen, D. J., Yau, A. W., Pilon, A. M., Cameron, T. A., Sebesta, J. F., ... Campbell, G. S. (1994, nov). The Freja F3C Cold Plasma Analyzer. *Space Science Reviews*, *70*(3-4), 541–561. Retrieved from http://link.springer.com/10.1007/BF00756885 doi: 10.1007/BF00756885

Yang, Y.-M., Garrison, J. L., & Lee, S.-C. (2012, jan). Ionospheric disturbances observed coincident with the 2006 and 2009 North Korean underground nuclear tests. *Geophysical Research Letters*, *39*(2), n/a–n/a. Retrieved from http://doi.wiley.com/10.1029/2011GL050428 doi: 10.1029/2011GL050428

Yau, A. W., Garbe, G. P., Greffen, M. J., Miyake, W., & Sagawa, E. (1998, mar). Planned observations of thermal plasma drifts and solar wind interactions in the Martian ionosphere. *Earth, Planets and Space*, *50*(3), 195–198. Retrieved from http://earth-planets-space.springeropen.com/articles/10.1186/BF03352103 doi: 10.1186/BF03352103

Yau, A. W., Howarth, A., White, A., Enno, G., & Amerl, P. (2015). Imaging and Rapid-Scanning Ion Mass Spectrometer (IRM) for the CASSIOPE e-POP Mission. *Space Science Reviews*, *189*(1-4), 41–63. Retrieved from http://dx.doi.org/10.1007/s11214-015-0149-8 doi: 10.1007/s11214-015-0149-8